(1995); L. Torsi, A. Dodabalapur, L. J. Rothberg, A. W. P. Fung, H. E. Katz, *ibid.* **272**, 1462 (1996).
7. Y. Yang and A. J. Heeger, *Nature* **372**, 344 (1994).
8. Q. Pei, G. Yu, C. Zhang, Y. Yang, A. J. Heeger, *Science* **269**, 1086 (1995); Q. Pei, Y. Yang, G. Yu, C. Zhang, A. J. Heeger, *J. Am. Chem. Soc.* **118**, 3922 (1996); Y. Cao, G. Yu, A. J. Heeger, C. Y. Yang, *Appl. Phys. Lett.* **68**, 3218 (1996).
9. D. Moses, *Appl. Phys. Lett.* **60**, 3215 (1992).
10. F. Hide, B. J. Schwartz, M. A. Díaz-García, A. J. Heeger, *Chem. Phys. Lett.* **256**, 424 (1996).
11. M. Yan, L. J. Rothberg, E. W. Kwock, T. M. Miller, *Phys. Rev. Lett.* **75**, 1992 (1995).
12. M. Yan *et al.*, *ibid.* **72**, 1104 (1994); R. Kersting *et al.*, *ibid.* **70**, 3820 (1993); W. Graupner *et al.*, *ibid.* **76**, 847 (1996); T. Pauck *et al.*, *Chem. Phys. Lett.* **244**, 171 (1995).
13. B. J. Schwartz, F. Hide, M. R. Andersson, A. J. Heeger, in preparation.
14. C. Zhang, S. Höger, K. Pakbaz, F. Wudl, A. J. Heeger, *J. Electron. Mater.* **22**, 413 (1993); C. L. Gettinger, A. J. Heeger, J. M. Drake, D. J. Pine, *J. Chem. Phys.* **101**, 1673 (1994).
15. Y. Yang, Q. Pei, A. J. Heeger, *J. Appl. Phys.* **79**, 934 (1996).
16. Q. Pei and Y. Yang, *J. Am. Chem. Soc.* **118**, 7416 (1996). For past polyfluorene work, see Y. Ohmori, M. Uchida, C. Morishima, A. Fujii, K. Yoshino, *Jpn. J. Appl. Phys.* **32**, L1663 (1993).
17. We have chosen the full-width at 1/*e* height to represent the linewidth of the emission spectra because this is more suitable (compared to other definitions such as FWHM) for comparison of disparate emission spectra with varying magnitudes of vibronic features.
18. P. R. Hammond, *Opt. Commun.* **29**, 331 (1979).
19. Among the PPV derivatives are several copolymers synthesized from varying ratios of BuEH-PPV and MEH-PPV monomers.
20. Details of film preparation and characterization will be reported elsewhere; B. J. Schwartz, M. A. Díaz-García, F. Hide, A. J. Heeger, in preparation.
21. We thank Z. V. Vardeny for making this point clear.
22. Polymer refractive indices were determined from the waveguide modal characterization by the prism coupling technique. We also note that the polymer films are birefringent and have a higher index in the plane of the substrate, which is indicative of partial chain alignment. See (*20*) for details.
23. H. Kogelnik, in *Topics in Appl Optics: Integrated Optics*, T. Tamir, Ed. (Springer-Verlag, Berlin, 1979), vol. 7, chap. 2.
24. Although absolute measurements of the PL quantum efficiency are difficult because the films are acting as waveguides, the integrated area of the PL data in Fig. 1 increases sublinearly at high pump energies. This sublinear increase might arise from excitation quenching at high excitation densities above threshold (*28*).
25. D. Shamrakov and R. Reisfeld, *Chem. Phys. Lett.* **213**, 47 (1993).
26. M. Kuwata-Gonokami *et al.*, *Opt. Lett.* **20**, 2093 (1995).
27. J. Grüner, F. Cacialli, R. H. Friend, *J. Appl. Phys.* **80**, 207 (1996); V. Cimrová and D. Neher, *ibid.* **79**, 3299 (1996); M. Berggren *et al.*, *Synth. Met.* **76**, 121 (1996); T. A. Fisher *et al.*, *Appl. Phys. Lett.* **67**, 1355 (1995); H. F. Wittman *et al.*, *Adv. Mater.* **7**, 541 (1995).
28. R. H. Friend, paper presented at the International Conference on Science and Technology of Synthetic Metals (ICSM '96), Snowbird, UT, 31 July 1996.
29. I. D. Parker, *J. Appl. Phys.* **75**, 1656 (1994).
30. D. Braun, D. Moses, C. Zhang, A. J. Heeger, *Appl. Phys. Lett.* **61**, 3092 (1992).
31. We thank G. Yu and Y. Yang (UNIAX Corp.) for valuable assistance and discussions, and UNIAX Corp. for making the Dektak surface profilometer available. Supported by the Office of Naval Research (N00014-91-J-1235). M.A.D.-G. is supported by the Government of Spain. M.R.A. thanks the Swedish Natural Science Research Council for support.

12 July 1996; accepted 27 August 1996

Nanorod-Superconductor Composites: A Pathway to Materials with High Critical Current Densities

Peidong Yang and Charles M. Lieber*

Most large-scale applications of the high-temperature copper oxide superconductors (HTSCs) require high critical current densities (J_c's) at temperatures near the boiling point of liquid nitrogen to be technologically useful, although thermally activated flux flow reduces J_c dramatically at these temperatures. This intrinsic limitation can be overcome by introducing nanometer-sized columnar defects into an HTSC. Nanorods of magnesium oxide were grown and incorporated into HTSCs to form nanorod-HTSC composites. In this way, a high density of nanorod columnar defects can be created with orientations perpendicular and parallel to the copper oxide planes. The J_c's of the nanorod-HTSC composites are enhanced dramatically at high temperatures and magnetic fields as compared with reference samples; these composites may thus represent a technologically viable strategy for overcoming thermally activated flux flow in large-scale applications.

Large J_c's are essential to many proposed applications of HTSCs, such as wires for power transmission cables and solenoids (*1*, *2*). In general, J_c is limited by two major factors (*1*, *3*, *4*). First, J_c is limited by thermally activated flux creep; that is, J_c vanishes well below the upper critical field line $H_{c2}(T)$ (which depends on temperature T) as a result of the motion of magnetic flux lines. This limitation is intrinsic and arises from the short coherence lengths and large anisotropies of the HTSC materials that lead to a weak pinning of flux lines (*3*–*6*). Second, in polycrystalline materials, J_c is limited by the alignment of the interfaces between superconducting grains: poor alignment of the grains and chemical heterogeneity at their boundaries produces weak links with low values of J_c (*3*, *7*). Progress has been made in improving the alignment of grains and consequently improving J_c's in wires and tapes based on $Ag\text{-}Bi_2Sr_2Ca_{n-1}Cu_nO_{2n+4}$ (n = 2, BSCCO-2212; n = 3, BSCCO-2223) through investigations of the effects of different material processing conditions on microstructure and on microscopic and macroscopic transport currents (*3*, *8*–*10*). Despite this progress in processing, which is now yielding BSCCO-based wires with J_c values sufficiently high to be considered for some commercial applications (*9*), the intrinsic problem of thermally activated flux creep continues to limit the performance of BSCCO materials at high T and H (*11*–*13*).

Theoretical (*14*, *15*) and experimental (*16*, *17*) studies have shown, however, that this problem in HTSCs can be reduced by creating correlated defects, such as columnar defects, in the crystal lattice. The interaction of flux lines with columnar defects results in a large pinning energy that effectively resists thermally activated flux motion and thus increases J_c significantly at high T and H (*14*, *18*). These linelike defects are usually created by irradiating samples with heavy ions having energies on the order of a gigavolt (Fig. 1). This procedure yields damage tracks 10 to 20 nm in diameter and tens of micrometers in length (*19*). The small defect diameter is essential to maximize the flux line core-pinning interaction without destroying an unneces-

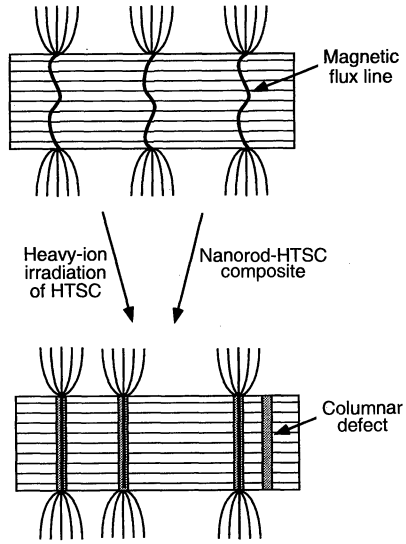

Fig. 1. Schematic diagram illustrating magnetic flux lines in an HTSC before and after the creation of columnar defects. The linear columnar defects strongly trap or pin the flux lines in the superconductor.

P. Yang, Department of Chemistry, Harvard University, Cambridge, MA 02138, USA.
C. M. Lieber, Division of Applied Sciences and Department of Chemistry, Harvard University, Cambridge, MA 02138, USA.

*To whom correspondence should be addressed.

sary volume fraction of the superconductor. Although heavy-ion–generated columnar defects can enhance J_c (*16*, *17*), large-scale applications are limited by the short penetration depth of heavy ions and the low thermal stability of the defects (*20*). These factors eliminate the possibility of producing columnar defects in processed wires or of forming wires from irradiated BSCCO powders, respectively. However, high-energy (0.8 GeV) protons can be used to create isotropic columnar damage tracks in BSCCO materials through the fission of Bi nuclei (*21*, *22*). The advantage of this approach is the large, 0.5-m penetration depth of the energetic protons that makes possible the production of columnar defects in completed wire cables. The fission process does, however, produce an isotropic distribution of defects that reduces the pinning efficiency of the columnar defects (*15*). Regardless of fundamental limitations, it is unclear whether high-energy, ion-irradiation techniques are economically viable for large-scale commercial applications.

The large enhancement of J_c produced by columnar defect structures argues that other strategies should be considered for their creation in HTSC materials (*23*). For example, the incorporation of rodlike nanostructures into an HTSC matrix should yield the same beneficial effect as ion-generated columnar defects. There are, however, several critical constraints to achieving a useful columnar defect structure in a composite: (i) the rodlike structures must have dimensions comparable to ion damage tracks (that is, nanorods), (ii) the nanorod should be chemically inert in the aggressive metal oxide environment used to prepare HTSCs, and (iii) the nanorod should be oriented, not isotropically distributed, within the superconducting matrix. From the perspective of size, carbon nanotubes are materials that might be considered for creating columnar defects (*24*). Carbon nanotubes are, however, very reactive in the oxygen–metal oxide environments needed to prepare high-quality samples (that is, they oxidize to form CO_2 gas) and thus are not useful for introducing a high density of well-defined columnar defects (*25*).

On the other hand, micrometer-diameter MgO whiskers can be incorporated into BSCCO superconductors with little chemical reaction (*26*, *27*). These micrometer-sized whiskers improve mechanical strength, but J_c does not appear to be enhanced and in some cases is lowered by their addition (*27*). We grew single-crystal MgO whiskers with nanometer-sized diameters [that is, nanorods (*28*)] and controlled their orientation when incorporated into thick-film and bulk BSCCO superconductor samples. The resulting nanorod-BSCCO composites showed enhancements in J_c similar to those produced previously by high-energy ion irradiation. Our approach to overcoming the intrinsic limitation of thermally activated flux creep can be implemented in processes currently used to produce large-scale HTSC samples and thus might affect applications such as power transmission cables.

Nanorods of MgO were grown with a modified vapor-solid growth process in which Mg vapor generated in situ through carbothermal reduction of MgO was transported in a flow reactor to a growth zone where nucleation and reoxidation (to MgO) occurred (*29*). The critical nucleation step determining the growth of MgO rods with nanometer-scale diameters can be reproducibly controlled with MgO nanoclusters 5 to 8 nm in diameter (*30*) or by chemical etching of MgO (100) single-crystal surfaces (*31*). Low-magnification transmission electron microscopy (TEM) images show that the MgO nanorods were straight or gently curved and ranged in diameter from 5 to 50 nm with a mean of ~20 nm; the lengths typically exceeded 2 μm (Fig. 2A). These dimensions are ideally suited for pinning magnetic flux lines in the HTSCs. High-resolution imaging and electron-diffraction measurements made on individual nanorods showed that these materials were single-crystal, cubic MgO with a [001] rod axis (Fig. 2B). As discussed below, this growth habit promotes the specific orientation of nanorods within bulk HTSC samples through lattice epitaxy.

Scanning electron microscopy (SEM) images recorded on etched MgO single crystals showed that a high density of oriented MgO nanorods can be produced on planar substrates (Fig. 2C). The principle growth direction of the nanorods was normal to the substrate surface, leading to a dense forest of rods with average diameters of 20 to 30 nm. We also observed some nanorods with their growth axes at a ~45° angle relative to the substrate surface. These two distinct orientations can be readily seen in a stereo view (Fig. 2C). The density of nanorods normal to the substrate surface in Fig. 2C is $\sim 3 \times 10^9$ cm^{-2}, although higher and lower densities can be achieved through variations in the initial substrate-etching conditions. TEM analysis of individual nanorods removed from the substrate surface showed that the rods have the same single-crystal structure and growth habit as described above.

We prepared and characterized nanorod-HTSC composites formed from substrate-aligned or bulk MgO nanorods and BSCCO-2212. The creation of columnar defects with the MgO nanorod approach is applicable to other HTSC systems as well (*32*). In general, high-quality nanorod-BSCCO composites and reference BSCCO samples have been made through use of standard melt-texturing procedures (*20*, *33*) that produce polycrystalline samples with well-oriented (textured) grains. In the present study, the substrate-aligned nanorod-BSCCO thick-film composites were made in a two-step process involving room-temperature laser deposition of 1- to 2-μm-thick amorphous BSCCO onto the forest of nanorods, followed by a partial melting and cooling cycle to crystallize the BSCCO ma-

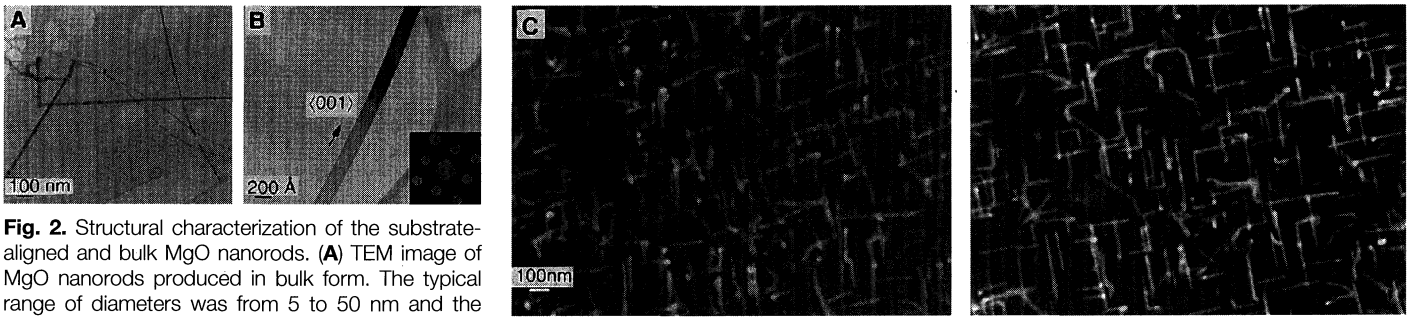

Fig. 2. Structural characterization of the substrate-aligned and bulk MgO nanorods. (**A**) TEM image of MgO nanorods produced in bulk form. The typical range of diameters was from 5 to 50 nm and the average was ~20 nm; the lengths were typically ≥2 μm. (**B**) High-resolution TEM image of a single nanorod 15 nm in diameter. The ⟨001⟩ growth axis was determined from convergent-beam electron-diffraction measurements (inset) taken perpendicular to the nanorod axis. (**C**) Stereomicrograph of MgO nanorods grown on a (100) MgO substrate surface (*39*). These SEM images demonstrate that the principle orientation of the rods was perpendicular to the substrate surface and that the average diameter of the rods was 25 nm. The areal density calculated from the micrographs is 3×10^9 cm^{-2}.

terial; reference BSCCO samples on MgO substrates were made with the same procedure. The x-ray diffraction studies of the films show that the partial melting-cooling cycle leads to crystalline, textured BSCCO-2212 in which the crystallographic *c* axis is normal to the substrate surface. Rocking curve analysis of the composite and reference samples further shows that the nanorods do not adversely affect the development of a well-textured polycrystalline product.

The columnar defect structure in the nanorod-BSCCO composite is seen clearly in SEM and TEM images (Fig. 3). First, low-magnification side-view images of the amorphous nanorod-BSCCO composites exhibit a columnar morphology that reflects deposition around the forest of nanorods (Fig. 3A); the reference samples do not exhibit a columnar morphology under similar magnification. Second, after melting and crystallization, SEM and TEM images demonstrate that the BSCCO matrix develops its characteristic platelike morphology and that there is a relatively high density of individual nanorods protruding from fractured samples (Fig. 3, B and C). High-resolution imaging of small BSCCO grains fractured from the substrate further show that the MgO nanorods are oriented nearly parallel to the BSCCO *c* axis. The size and density of nanorods in the BSCCO matrix has been estimated from the analysis of in-plane TEM images recorded on thinned samples. A relatively high density of dark, roughly circular spots with diameters of 20 to 30 nm is seen in images of the composite crystal grain (Fig. 3D). The density, about 2×10^9 cm^{-2} (*34*), and size of the features in the composite correspond well to the values determined for the nanorods before formation of the composite. Spatially resolved elemental analysis by energy-dispersive x-ray spectroscopy (EDAX) shows that these 20- to 30-nm features contain primarily Mg with only trace amounts of Sr and Cu from the BSCCO matrix. Taken together, these data show that a relatively high density of MgO nanorod columnar defects can be made in BSCCO HTSCs.

Similar results were also obtained for the formation of nanorod-BSCCO composites on silver tapes. In this case, the composites were prepared by (i) mixing bulk MgO nanorods with prereacted BSCCO-2212 powder and (ii) partially melting a nanorod-BSCCO pellet made from the mixture on a piece of silver foil. X-ray diffraction measurements made on both composite and reference samples showed only the (001) reflections of BSCCO-2212, thus showing good texture of the BSCCO grains within these samples. More importantly, TEM analyses of these samples showed that a high density of MgO nanorods was incorporated into the crystalline grains (Fig. 3, E and F). Images recorded with the electron beam along the *c* axis (in-plane structure) showed roughly circular, dark spots with diameters of ~30 nm that contained primarily Mg. These features are similar to those observed for the samples containing substrate-oriented nanorods (above) and thus suggest that many nanorods preferentially orient along the BSCCO *c* axis in these silver tape samples. The columnar structure and near *c* axis orientation was further confirmed by tilting (Fig. 3F) and cross-sectional TEM studies of the composites.

Systematic TEM analysis of the nanorod orientation in the composites formed on silver foil showed that there are two preferred orientations: parallel and perpendicular to the *c* axis; that is, the nanorods are not oriented isotropically in these samples (*35*). We believe the preferred orientation or self-organization of the MgO nanorods after melt-texturing occurs because the exposed MgO surfaces are lattice-matched substrates for the growth of BSCCO with either the *a* and *b* axes or the *c* axis oriented perpendicular to the nanorod axis. Hence, the synthesis of MgO nanorods serves a dual purpose: This oxide minimizes deleterious reactions with the HTSC matrix, and the structure leads to self-organization within BSCCO. Because oriented columnar defects are expected to produce improved values of J_c compared with an isotropic distribution (*15*), we believe that the observed self-orientation of MgO nanorods during composite processing is significant for applications.

We systematically characterized J_c in the nanorod-BSCCO composites and BSCCO reference samples through measurements of the sample magnetization M as a function of H and T. The sample $J_c(H,T)$ is simply related to the hysteresis in magnetization, $\Delta M(H,T)$, by a geometric factor, assuming that supercurrents flow within the entire sample: $J_c = 15\Delta M/R$, where R is the radius of the entire sample (*36*). Although this approach could underemphasize the limitation of grain boundaries on J_c, it is appropriate for probing the intrinsic effects of defect pinning that are the focus of our studies (*11*, *21*). The H dependence of J_c data determined at several temperatures for reference and composite samples (Fig. 4A)

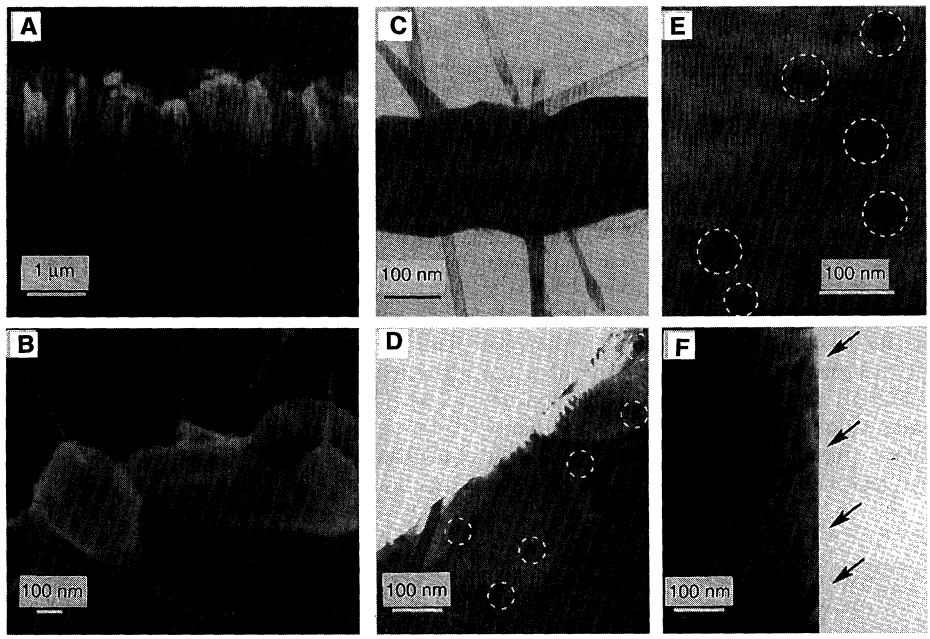

Fig. 3. Structural characterization of the BSCCO-nanorod composites (*40*). (**A**) An SEM cross-sectional image of the substrate-aligned nanorod composite after room-temperature deposition. The columnar structure of the amorphous BSCCO (vertical direction) is seen in this image. (**B**) SEM image of the same sample after melt-texturing. The platelike morphology, which is typical of crystalline BSCCO, is seen in this cross section. In addition, several nanorods can be seen protruding from the upper surface of the grain. In both (A) and (B) the MgO substrate is located at the bottom of the image. (**C**) Cross section and (**D**) in-plane TEM images recorded on a substrate-aligned nanorod-BSCCO composite. The propagation of several ~20-nm-diameter MgO nanorods through a crystal grain is seen clearly in (C). The in-plane density estimated from images such as in (D) is 3×10^9 cm^{-2}; in this image the nanorods correspond to dark-filled circles, the composition of which was verified with EDAX. (**E**) In-plane TEM image of bulk BSCCO-nanorod composite. The MgO nanorods perpendicular to the copper oxide planes correspond to the darker, roughly circular spots. The columnar nature of these defects was verified by tilting the sample off axis (**F**). Four MgO nanorod columnar defects are highlighted with black arrows.

is typical of that obtained for the composite and reference samples. In general, the nanorod-BSCCO composites exhibit large increases in J_c compared with the reference samples, and these increases are especially significant at higher H and T. Because the J_c values of our BSCCO-2212 reference samples are comparable to the best reported for polycrystalline thick films (*17*, *21*), we believe that the increases observed in the nanorod composites are not an artifact of our chosen reference point.

The large increases in J_c are attributed to enhanced pinning arising from nanorod columnar defects in our composite samples. Several pieces of evidence support this proposal. First, the increases in $J_c(H,T)$ become more pronounced with increasing H and T. These results at elevated H and T are characteristic of the behavior expected for pinning by columnar defects and cannot be explained by point-defect pinning, which characteristically shows little effect above 30 K. In addition, the enhancement in J_c exhibits an inverse dependence on the average diameter of the nanorods (Fig. 4B). These results are consistent with expectations for optimal pinning (*14*) and also show the importance of developing small nanorods for the HTSC composites (*37*). Last, the importance of the columnar defects created by the nanorods was further checked by making composites with spherical MgO nanoclusters. Although these nanocluster composites exhibited increased values of J_c compared with those of reference samples at low temperatures, the nanocluster composite and reference samples had comparable behavior at temperatures >25 K.

We examined the T dependence of J_c for selected H values to evaluate potential high-temperature applications. Results obtained on nanorod-BSCCO composites and reference samples at H = 0.2 and 0.5 T are shown (Fig. 5). In the reference samples, J_c fell off rapidly with T as a result of thermally activated flux flow. In the nanorod-BSCCO composites, however, this rapid fall-off was dramatically reduced and led to improvements in J_c that could exceed one order of magnitude. The large increases in $J_c(H,T)$ for the nanorod-BSCCO composites can also be summarized by a plot in the H-T plane of the irreversibility line; that is, the line that defines reversible compared with irreversible behavior in the superconductor (Fig. 6). From the standpoint of applications, the operating H and T must be chosen to be below this line because dissipation (that is, loss of superconductivity) occurs above it. Large upward shifts in the irreversibility line for the nanorod-BSCCO composites of 10 and 20 K occur at fields of 0.5 and 1.0 T, respectively. We can thus conclude that the potential operating regime is extended for nanorod-BSCCO composites.

We can compare our results with those obtained previously in samples containing columnar defects generated by heavy-ion and proton irradiation. In general, the enhancements in J_c and the shift of the irreversibility line found in the nanorod-BSCCO composites are comparable to those observed previously in ion-irradiated samples (*17*, *21*, *22*). The maximum density of nanorod defects that we achieved, however, corresponds to an effective field of 0.25 T, which is much lower than that achieved by ion irradiation. Although the true density of correlated defects in the composites is probably greater than this number (*34*), the nanorod density will need to be increased to extend the range of fields for which strong pinning is observed. However, we believe that the ability to make samples with strong-pinning columnar defects by our composite approach has distinct advantages over irradiation with giga–electron volt protons for large-scale applications because current methods of processing should be usable with little modification.

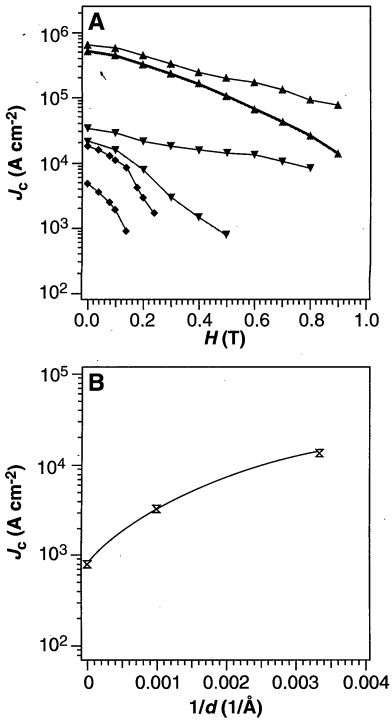

Fig. 4. (**A**) Comparison of the H dependence of J_c for BSCCO-nanorod composite (red) and BSCCO reference (blue) samples; the T_c's of both samples were 80 K. The data shown correspond to measurements made at 5 (▲), 40 (▼), and 60 K (◆). (**B**) Dependence of J_c as a function of the average diameter of nanorods incorporated into the BSCCO matrix. The point at $1/d$ = 0 corresponds to a reference sample without nanorods. All results correspond to a T = 40 K and H = 0.5 T parallel to the c axis. The J_c results were determined from magnetization hysteresis loops with the Bean model (*36*). The hysteresis loops were recorded with H parallel to the c axis of the samples (MPMS2, Quantum Design). The solid lines through the points in (A) and (B) are guides to the eye.

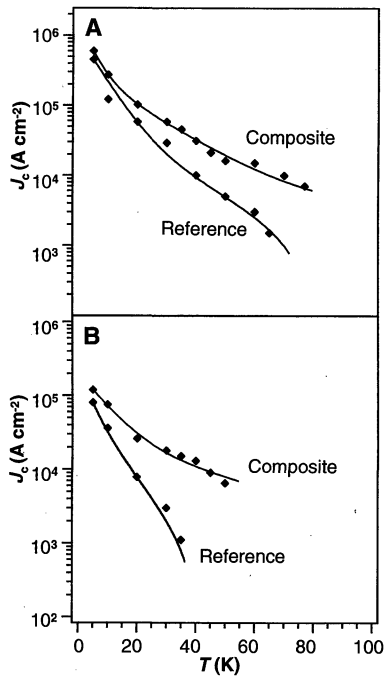

Fig. 5. Comparison of the T dependence of J_c in a typical BSCCO-nanorod composite and our best BSCCO reference samples at (**A**) 0.1 T and (**B**) 0.5 T. Both samples had a T_c of ~80 K. The solid lines are guides to the eye.

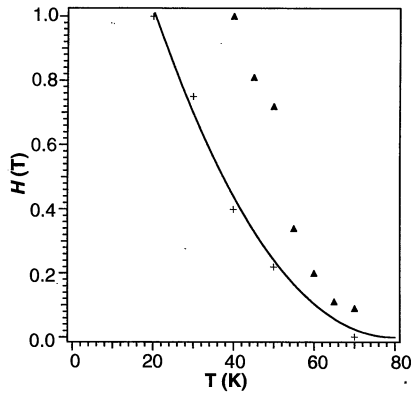

Fig. 6. Plots of the irreversibility line for BSCCO-nanorod composite (▲) and BSCCO reference (+) samples. Both samples had a T_c of ~80 K. The irreversibility line for the BSCCO-nanorod composite exhibits a broad discontinuity at a value of H similar to the equivalent density of columnar defects. The irreversibility point was taken as the field at which the hysteresis loop closed for each temperature (*21*). For our experiments, the closing criterion was taken to be 5×10^{-6} electromagnetic units and was applied to similar-sized composite and reference samples in the analysis. The solid line corresponds to a fit to $H_{irr} \propto (-T_{irr}/T_c)^n$, where the subscript "irr" refers to irreversible and n ~ 2.08.

REFERENCES AND NOTES

1. G. B. Lubkin, *Phys. Today* **49**, 48 (March 1996); D. C. Larbalestier and M. P. Maley, *Mater. Res. Soc. Bull.* **18**, 50 (1993).
2. P. M. Grant, *Nature* **375**, 107 (1995).
3. A. E. Pashitski, A. Polyanskii, A. Gurevich, J. A. Parrell, D. C. Larbalestier, *Physica C* **246**, 133 (1995).
4. D. J. Bishop, P. L. Gammel, D. A. Huse, C. A. Murray, *Science* **255**, 165 (1992).
5. D. S. Fisher, M. P. A. Fisher, D. A. Huse, *Phys. Rev. B* **43**, 130 (1991).
6. G. Blatter, M. V. Feigel'man, V. B. Geshkenbein, A. I. Larkin, V. M. Vinokur, *Rev. Mod. Phys.* **66**, 1125 (1994).
7. A. P. Malozemoff, in *Physical Properties of High Temperature Superconductors*, D. Ginsberg, Ed. (World Scientific, Singapore, 1989), pp. 71–150.
8. U. Welp *et al.*, *Nature* **376**, 44 (1995).
9. W. L. Carter *et al.*, *IEEE Trans. Appl. Supercond.* **5**, 1145 (1995); C. J. Christopherson and G. N. Riley Jr., *Appl. Phys. Lett.* **66**, 2277 (1995); K. Sato *et al.*, *Physica B* **216**, 258 (1996); K. Ohkura, K. Sato, M. Ueyama, J. Fujikami, Y. Iwasa, *Appl. Phys. Lett.* **67**, 1923 (1995).
10. D. C. Larbalestier *et al.*, *Physica C* **221**, 299 (1994); M. Lelovic, P. Krishnaraj, N. G. Eror, U. Balachandran, *ibid.* **242**, 246 (1995).
11. Q. Li, H. J. Wiesmann, M. Suenaga, L. Motowidlo, P. Haldar, *Appl. Phys. Lett.* **66**, 637 (1995).
12. P. Majewski, *Adv. Mater.* **6**, 593 (1994).
13. The problem of thermally activated flux motion is less severe in the HTSC $YBa_2Cu_3O_7$ (YBCO) and hence it offers better intrinsic behavior at high temperatures and magnetic fields. The processing strategies developed for BSCCO fail to yield viable YBCO wires as a result of poor intergranular current flow. Recent work suggests, however, that good alignment between grains can be achieved in thick films deposited on nickel tapes by ion beam deposition [X. D. Wu *et al.*, *Appl. Phys. Lett.* **67**, 2397 (1995)]. The commercial viability of this strategy remains to be demonstrated.
14. D. R. Nelson and V. M. Vinokur, *Phys. Rev. Lett.* **68**, 2398 (1992); ———, *Phys. Rev. B* **48**, 13060 (1993).
15. T. Hwa, P. Le Doussal, D. R. Nelson, V. M. Vinokur, *Phys. Rev. Lett.* **71**, 3545 (1993).
16. L. Civale *et al.*, *ibid.* **67**, 648 (1991); M. Konczykowski *et al.*, *Phys. Rev. B* **44**, 7167 (1991); R. C. Budhani, M. Suenaga, S. H. Liou, *Phys. Rev. Lett.* **69**, 3816 (1992); W. Gerhauser *et al.*, *ibid.*, **68**, 879 (1992); J. R. Thompson *et al.*, *Appl. Phys. Lett.* **60**, 2306 (1992); L. Civale *et al.*, *Physica C* **208**, 137 (1993).
17. P. Kummeth *et al.*, *J. Alloys Compd.* **195**, 403 (1993); P. Kummeth, C. Struller, H.-W. Neumuller, G. Saemann-Ischenko, *Appl. Phys. Lett.* **65**, 1302 (1994).
18. H. Dai, S. Yoon, J. Liu, R. C. Budhani, C. M. Lieber, *Science* **265**, 1552 (1994); U. C. Tauber, H. Dai, D. R. Nelson, C. M. Lieber, *Phys. Rev. Lett.* **74**, 5132 (1995).
19. Y. Zhu, Z. X. Cai, R. C. Budhani, M. Suenaga, D. O. Welch, *Phys. Rev. B* **48**, 6436 (1993).
20. J. R. Thompson, D. Paul, Z. L. Wang, D. M. Kroeger, D. K. Christen, *Appl. Phys. Lett.* **67**, 1007 (1995).
21. L. Krusin-Elbaum *et al.*, *ibid.* **64**, 3331 (1994).
22. H. Safar *et al.*, *ibid.* **67**, 130 (1995).
23. P. Le Doussal and D. R. Nelson, *Physica C* **232**, 69 (1994).
24. K. Fossheim, E. D. Tuset, T. W. Ebbesen, M. M. J. Treacy, J. Schwartz, *ibid.* **248**, 195 (1995).
25. A recent report of carbon nanotube-BSCCO composites (*24*) showed some evidence of J_c improvement; however, the J_c value of both the reference and nanorod-containing sample in this report were lower than the good-quality BSCCO samples reported previously and in the present study. It is thus difficult to conclude that there is an improvement in behavior upon adding nanotubes. In addition, this report and our own studies show that few nanotubes survive the synthesis process, leaving in doubt their ability to create well-defined columnar defects in the HTSCs.
26. N. Adamopoulos, B. Soylu, Y. Yan, J. E. Evetts, *Physica C* **242**, 68 (1995).
27. Y. S. Yuan, M. S. Wong, S. S. Wang, *J. Mater. Res.* **11**, 8 (1996); *Physica C* **250**, 247 (1995).
28. H. Dai, E. W. Wong, Y. Z. Lu, S. Fan, C. M. Lieber, *Nature* **375**, 769 (1995).
29. P. Yang and C. M. Lieber, in preparation.
30. H. Itoh, S. Utamapanya, J. V. Stark, K. J. Klabunde, J. R. Schlup, *Chem. Mater.* **5**, 71 (1993).
31. K. Sangwal, *J. Mater. Sci.* **17**, 3598 (1982).
32. Nanorod-HTSC composites have also been successfully prepared with $TlBa_2Ca_2Cu_3O_9$ and $Tl_2Ba_2Ca_2Cu_3O_{10}$ materials. Preliminary measurements show that there are significant enhancements in J_c for these composites (P. Yang and C. M. Lieber, unpublished results).
33. C. Li, S. Patel, J. Ye, E. Narumi, D. T. Shaw, *Appl. Phys. Lett.* **63**, 2558 (1993).
34. The actual density of columnar defects that can pin flux lines may be larger than that corresponding to the density of MgO nanorods; that is, lattice strains associated with nanorod-BSCCO interfaces can lead to dislocations and other correlated defects that exhibit columnarlike pinning behavior.
35. The density of nanorods oriented close to the *c* axis was about 1×10^{10} cm^{-2}; a similar density was determined for nanorods oriented in the *ab* plane. Although this density is significantly lower than that obtained by heavy-ion and proton irradiation, we have not tried to maximize the density of MgO nanorods and also believe that the density of correlated defects is probably significantly higher than that of nanorods (*34*).
36. C. P. Bean, *Rev. Mod. Phys.* **36**, 31 (1964).
37. An inverse dependence of J_c on defect size was also reported previously for Y_2BaCuO_5 inclusions of 1 to 10 μm in diameter in YBCO [M. Murakami, in *Phenomenology and Applications of High-Temperature Superconductors*, K. S. Bedell, M. Inui, D. Meltzer, J. R. Schrieffer, S. Doniach, Eds. (Addison-Wesley, New York, 1992), p. 103].
38. A. Morales, P. Yang, C. M. Lieber, *J. Am. Chem. Soc.* **116**, 8360 (1994).
39. The MgO nanorods were grown as follows: a mixture of MgO (Alfa, 1 μm) and graphite powder (Alfa, 300 mesh), 1:3 to 3:1 weight ratio, was ground and placed in a graphite boat inside a quartz furnace tube. MgO nanoclusters 5 to 8 nm in diameter (*30*) or a MgO (100) single crystal, which had been etched with a $NiCl_2$ solution (*31*), was placed in a second graphite boat, and the tube was purged with Ar; the nucleation sites were located downstream of the MgO-carbon mixture. With the Ar flowing, the quartz tube was heated at a temperature of 1200°C for 0.5 to 2 hours and then cooled to room temperature. MgO nanorods were isolated from the graphite boat containing the MgO nanocluster or etched (100) MgO surface.
40. The amorphous BSCCO film was deposited at room temperature by laser ablation of a $Bi_{2.2}Sr_2CaCu_2O_x$ target in 200 mtorr of oxygen with a pulse energy of 1 J cm^{-2} (*38*). Bulk composites were made by (i) mixing BSCCO-2212 powder with MgO nanorods (~15% weight ratio), (ii) pressing the mixture into a pellet, and (iii) melt-texturing the resulting pellet on silver foil. The texturing procedure used to prepare both types consisted of partial melting at 860° to 880°C and then cooling to 780°C at a rate of 1° to 5°C hour^{-1}; after annealing at 780°C for 10 to 24 hours, samples were cooled to room temperature. The T_c's of composite and reference samples prepared in this way were typically 78 to 84 K.

41. We acknowledge helpful discussions with D. R. Nelson and F. Spaepen. This work was supported in part by the Materials Research Science and Engineering Center Program of the National Science Foundation (grant DMR 9400396) and the Office of Naval Research (grant N00014-94-1-0302).

7 May 1996; accepted 17 July 1996

Methane Hydrate and Free Gas on the Blake Ridge from Vertical Seismic Profiling

W. Steven Holbrook, Hartley Hoskins, Warren T. Wood, Ralph A. Stephen, Daniel Lizarralde, Leg 164 Science Party

Seismic velocities measured in three drill holes through a gas hydrate deposit on the Blake Ridge, offshore South Carolina, indicate that substantial free gas exists to at least 250 meters beneath the bottom-simulating reflection (BSR). Both methane hydrate and free gas exist even where a clear BSR is absent. The low reflectance, or blanking, above the BSR is caused by lithologic homogeneity of the sediments rather than by hydrate cementation. The average methane hydrate saturation above the BSR is relatively low (5 to 7 percent of porosity), which suggests that earlier global estimates of methane in hydrates may be too high by as much as a factor of 3.

Marine sediments can contain large quantities of natural gas (usually methane) in the form of gas hydrate, a solid compound binding water and gas molecules, which is stable at the high pressures and low temperatures found near the sea floor on continental margins (*1*, *2*). Gas hydrate deposits are identified principally on the basis of their acoustic expression: The phase boundary between methane hydrate and methane plus water gives rise to a prominent negative-polarity event known as a BSR (*3*, *4*), and the addition of hydrate to pore fluids has been interpreted to cause acoustic blanking, a suppression of sediment reflectivity (*5*, *6*). Knowledge of the amount and distribution of methane present as hydrates or free gas is crucial to understanding the potential of methane hydrates as an energy

W. S. Holbrook, H. Hoskins, R. A. Stephen, Department of Geology and Geophysics, Woods Hole Oceanographic Institution, Woods Hole, MA 02543, USA.
W. T. Wood, Naval Research Laboratory, Stennis Space Center, MS 39529, USA.
D. Lizarralde, Massachusetts Institute of Technology–Woods Hole Joint Program, Woods Hole Oceanographic Institution, Woods Hole, MA 02543, USA.